

Supplementary Materials for
A buckling-sheet ring oscillator for electronics-free, multimodal locomotion

Won-Kyu Lee *et al.*

Corresponding author: George M. Whitesides, gwhitesides@gmwgroup.harvard.edu

Sci. Robot. **7**, eabg5812 (2022)
DOI: [10.1126/scirobotics.abg5812](https://doi.org/10.1126/scirobotics.abg5812)

The PDF file includes:

Materials and Methods
Supplementary Text
Figs. S1 to S13
Tables S1 and S2
Legends for movies S1 to S12
References (37–40)

Other Supplementary Material for this manuscript includes the following:

Movies S1 to S12

Materials and Methods

Fabrication of buckling-sheet actuator and pneumatic inverter

Each buckling-sheet actuator was fabricated from a circular sheet of polycellulose acetate (Hygloss Products, Inc. overhead projector transparency sheets made from cellulose diacetate) with a diameter of 7 cm (**Fig. S1**). We attached a thin circular Nylon film (McMaster-Carr Nylon film, 0.005mm thick), with a diameter of 4 cm, to the center of the circular sheet using double-sided tape (3M 9589 double-sided tape) to form a pneumatic bladder. Thin tubing (McMaster-Carr PDMS tubing, 0.5 mm internal diameter) allows the bladder to attach to an external pneumatic source; we sealed the connection between the tubing and the cellulose acetate sheet with a hot-melt adhesive (Surebonder Glue Sticks, poly(amidoamine)) applied with a hot glue gun (Surebonder GM-160 Glue Gun, 10-watt). The transparency sheet and the Nylon bladder are both flexible but inextensible. When the bladder is pressurized, it expands in volume but contracts in diameter (due to its inextensible nature in the applied pressure range), applying stress to the entire transparency sheet. The cellulose acetate sheet releases stress by buckling out-of-plane. Upon the first actuation, the initial buckling instability created in the sheet occurs at a random position along the radial direction. When this buckled sheet is kept in the buckled state for a minute, the material develops a “buckling memory.” After this initial “programming” of the buckling position, the sheet always buckles reproducibly in the same location—it thus becomes a reliable actuator and could operate up to ~ 80 kPa without failure. We previously conducted a reliability test for the buckling-sheet actuators with cyclic actuation and confirmed that the devices are stable hundreds of cycles of pressurization and depressurization (26). To fabricate a pneumatic transistor from the buckling sheet, we attached a pneumatic flow-control tube with

reversible kinking composed of soft blue tubing (Smooth-On Smooth-Sil 950, 2 cm length, 3 mm inner diameter) connected on either side to the same PDMS tubing used to connect to the bladder (**Fig. S1**). The flow-control tubing was attached on the surface of buckling sheet, across the buckling position. We then attached the pneumatic pulldown resistor—a length of PDMS tubing with a small (0.8 mm) inner diameter to provide a resistance to airflow (**Fig. S7**). The pulldown resistor is required to create an inverter from the buckling-sheet transistor described above; without the pulldown resistor, the output state would always remain at the supply pressure after the first actuation.

Nonlinear finite element model for pneumatic inverter based on the buckling-sheet actuator

Nonlinear finite element method (FEM) modeling was employed to analyze the working principles of the buckling-sheet inverter (40), using the commercially available software package Abaqus (Version 2019, Dassault Systèmes, 175 Wyman Street, Waltham, MA 02451, United States). The global behavior of the buckling-sheet actuator was modeled by decoupling the bending of the sheet actuator from the buckling of a pneumatic flow-control tubing (**Fig. S4A**). This decoupling is justified since the structural stiffness of the buckling-sheet actuator is orders of magnitude higher than that of the elastomeric flow-control tubing. As a first step, the deformation upon pressurizing the pneumatic bladder of the buckling-sheet actuator was modeled while tracking the displacement of the attachment points of the flow-control tubing (**Fig. S4B, Movie S1**). To fix the location of the buckle on the buckling-sheet actuator, an imperfection was introduced in the geometry that matched the initial plastic programming done on the physical prototypes. All materials were modeled using a Neo-Hookean material model (39), where material parameters were determined experimentally by performing uniaxial tensile tests. In more detail, tensile tests on the materials

that make up the buckling-sheet inverter were done using an Instron 5969 universal testing machine with a 500 N load cell. The initial dimensions of the material specimens were measured using a caliper, where for the length the distance between the clamps of the tensile machine was taken (**Table S1**). The data of these tensile tests are depicted in **Fig. S13**. A linear regression was performed on the tensile data to determine Young's moduli of the different materials with values: 2.13GPa (acetate sheet), 0.32GPa (double-sided tape), 2.35GPa (Nylon film).

In addition, a small amount of material damping (Rayleigh damping with a damping coefficient of 0.2) was introduced in the material definition of the software. The circular sheets of polycellulose acetate, double-sided tape, and nylon film composing a buckling-sheet actuator were individually meshed using, in total, approximately 30,000 8-node brick linear elements (Abaqus element code C3D8H) and tied together to ensure structural lamination. Due to symmetry conditions, only half of the structure needed to be modeled. As a second step, the output displacement of the attachment points was used as a driving parameter to axially deform the flow-control tube while tracking the cross-sectional deformation of the central part of the tube (**Fig. S4C**, **Movie S2**), which is the location at which the kink forms (34). The tube was meshed using, in total, approximately 60,000 8-node brick linear elements (Abaqus element code C3D8R), and a Neo-Hookean material model. The results of both analyses were combined to generate the global behavior of the buckling-sheet inverter, as **Fig. S4D** shows. This analysis illustrates that the difference in threshold pressures between folding and unfolding originates largely from the small hysteretic behavior of the buckling-sheet actuator, which is enlarged by the significant nonlinear response of the tube due to the buckling-loading condition (34).

Preparation of untethered pneumatic source with a wireless control

We integrated a BRO with an on-board pneumatic source consisting of two micropumps and supporting control electronics to enable untethered robot locomotion (**Fig. S12**). The control circuitry of the untethered BRO consists of: (i) a microcontroller (Microchip ATMEGA168PA), (ii) a MOSFET (ON Semiconductor NTZD3154NT), (iii) a WiFi chip (XBee PRO S1), (iv) a voltage regulator (Microchip MIC5219), and (v) a rechargeable lithium-ion battery (Turnigy 7.4V, 300 mAh, 45-90C). For the autonomous movement of our oscillating robot, we used two SKOOCOM SC3101PM diaphragm pumps in series (purchased from Alibaba) controlled by the circuit board. The maximum pressure of a single micropump is 300 mmHg. It can be operated by applying a DC voltage between 3 V to 6 V, with corresponding currents between 150 mA and 350 mA.

Design and assembly of the beam-climber robot

The beam climber robot was fabricated by connecting a BRO to an additional three pairs of buckling-sheet actuators and mounting these actuators to four semi-soft styrene frames that grip a beam with silicone feet (**Figs. S10 and S11**). The three pairs of actuators connect the four frames, and each pair of actuators is controlled by a different output signal from the BRO, such that the forward pair, middle pair, and rear pair actuate separately but sequentially. As the BRO actuates each pair, the corresponding rear frame is pulled forward, and as each pair of actuators is depressurized, the actuators relax to their original length and push the corresponding front frame forward (**Fig. S12**). Motion along the beam can be achieved due to the anisotropic friction of the silicone feet, which contact the beam at a 45° angle. The styrene pieces (Plastruct Inc.,

white styrene plate, $12.1 \times 7.1 \times 0.18$ inches) and acetate pieces (Hygloss Products, Inc., overhead projector sheet acetate transparency film) were cut to size using a laser cutter (Universal Laser Systems Inc., VLS 6.60 with a 60-Watt CO₂ laser) or scissors, and the robot is held together with double-sided tape (3M 9589 double-sided tape), super glue (Elmer's Products, Inc., Krazy Glue) and a hot-melt adhesive (Surebonder Glue Sticks, poly(amidoamine)) applied with a hot-glue gun (Surebonder GM-160 Glue Gun, 10-watt). The semi-soft styrene frame was fabricated by laser cutting individual parts and gluing them together with the super glue and hot glue as shown in **Fig. S10**. Specifically, the silicone rubber feet (bundles of PDMS tubes 0.8 mm diameter) were attached to lengths of styrene using super glue (**Fig. S10A**). Then we glued (with hot glue) these lengths of styrene-PDMS composite to form rectangular frames (also made of styrene) that held the feet such that they contacted the beam at a 45° angle. We used four of these frames for one robot. To enable actuation, three pairs of buckling sheet actuators were mounted between the four frames. We mounted each actuator to the frame in front of it using the double-sided tape and an acetate sheet. We mounted each actuator to the frame behind it by gluing (using super glue) a thin piece of styrene along the “programmed” buckling position and gluing an acetate sheet between that piece of styrene and the frame (**Fig. S10B**). Finally, we mounted the three buckling-sheet inverters of the BRO directly onto the front three frames using double-sided tape, and we connected the corresponding pairs of actuators to each output pressure signal from the BRO as shown in **Fig. S11A-B**.

Supplementary Text

Analytical model for a BRO based on an analogous electronic circuit

We characterized the dependence of the period and the amplitude of the BRO on each of three adjustable system parameters: the supply pressure (P_{SUPP}), the pneumatic resistance from the pulldown resistor (R_{PULL}), and the inter-device pneumatic resistance (resulting from tubes connecting the buckling-sheet inverters; R_{TUBE}). Because the tubing volume is much smaller than the internal volume of the bladder in the actuator, we neglected compressibility along the tubing. We estimated a Reynolds number of $\text{Re} \sim 10\text{-}100$ for the gas (air), a much smaller value than the critical Reynolds number $\text{Re} \sim 2,300$ for transition to turbulent flow (37, 38). In **Figs. 2C-D**, we therefore modeled and calculated R_{TUBE} (or R_{PULL}) with the Darcy–Weisbach equation (38) for laminar flow (Eq. S1):

$$R_{\text{TUBE}} \text{ (or } R_{\text{PULL}}) = \frac{\Delta P}{\dot{m}} = \frac{128\mu L}{\pi\rho D^4} \quad (\text{S1})$$

In Eq. S1, ΔP (kPa) is the pressure difference between the ends of the tubing, \dot{m} (kg/s) the mass flow rate of air, μ (Pa-s) is the dynamic viscosity of air, ρ is the density of air at standard pressure and temperature, and D and L are the inner diameter and the length of the tubing. Meanwhile, the shape of the tubing and the volume of pneumatic bladder of the buckling-sheet inverter itself depend on its deformation during the oscillation consisting of cyclic buckling-unfolding states. We therefore determined the characteristic pneumatic resistance (R_{BSA}) and capacitance (C_{BSA}) of the buckling-sheet inverter by determining the best fit of the final equation to the experimental data with these quantities used as fitting parameters.

To derive an equation for the oscillation period as a function of P_{SUPP} , R_{PULL} , and R_{TUBE} , and the number of inverters in the ring n , we modeled the airflow between two adjacent inverters that are in the same state of actuation, during both buckling and unfolding (**Figs. S8A and S8B**,

respectively), and extended the result to the entire ring oscillator. The oscillation period of a BRO containing n inverters (t_{PERIOD}) is the sum of the buckling times (t_{B}) and unfolding times (t_{U}) of all n buckling-sheet inverters.

During buckling, air flows from the pressure supply (P_{SUPP}) through the resistor (R_{TUBE}) to the bladder of buckling-sheet inverter (C_{BSA}) and to the atmosphere (P_{ATM}) through the pulldown resistor (R_{PULL}) simultaneously (**Fig. S7A**). Equation S2 from the analogous electronic RC circuit describes the time-varying pressure $P(t)$ inside the bladder of the buckling-sheet inverter:

$$\frac{dP}{dt} = \frac{1}{R_{\text{TUBE}} \times C_{\text{BSA}}} \times (P_1 - P(t)) \quad (\text{S2})$$

where P_1 is:

$$P_1 = \left(\frac{1}{\frac{1}{R_{\text{PULL}}} + \frac{1}{R_{\text{BSA}}} + \frac{1}{R_{\text{TUBE}}}} \right) \times \left(\frac{P_{\text{SUPP}}}{R_{\text{BSA}}} + \frac{P_{\text{ATM}}}{R_{\text{PULL}}} + \frac{P(t)}{R_{\text{TUBE}}} \right) \quad (\text{S3})$$

In Eq. (S2), dP/dt is the derivative of $P(t)$ with respect to time during the buckling, i.e., from unfolded state ($P(t)$ below P_{UNFOLD}) to buckled state ($P(t)$ above P_{BUCK}). Notably, the minimum output pressure was slightly below P_{UNFOLD} , not P_{ATM} , because the bladder starts to inflate right after the buckling-sheet inverter is unfolded (when pressure inside bladder is still near P_{UNFOLD} ; initial condition for **Fig. S7A**, State 1). Solving the differential equation with the boundary condition of $P(t=0) = P_{\text{UNFOLD}}$ resulted in the solution of $P(t)$ summarized by Equation S4:

$$P(t) = (P_{\text{EFF}} - P_{\text{UNFOLD}}) \times \exp\left(-t/(R_{\text{EFF}} \times C_{\text{BSA}})\right) + P_{\text{EFF}} \quad (\text{S4})$$

Where the effective pressure (P_{EFF}) of the system captures the contributions of both the atmospheric and supply pressures, and the effective pneumatic resistance (R_{EFF}) of the circuit accounts for contributions from the three relevant pneumatic resistances: (i) the pulldown resistor, (ii) the inter-device pneumatic resistance, and (iii) the pneumatic resistance of the flow-control tubing on a buckling-sheet actuator (R_{BSA} and C_{BSA} indicate the intrinsic pneumatic resistance and capacitance from the individual buckling-sheet actuator (BSA), respectively):

$$P_{\text{EFF}} = \frac{P_{\text{SUPP}} \times R_{\text{PULL}} + P_{\text{ATM}} \times R_{\text{BSA}}}{R_{\text{PULL}} + R_{\text{BSA}}} \quad (\text{S5})$$

$$R_{\text{EFF}} = \frac{R_{\text{TUBE}} \times R_{\text{BSA}} + R_{\text{PULL}} \times R_{\text{BSA}} + R_{\text{PULL}} \times R_{\text{TUBE}}}{R_{\text{PULL}} + R_{\text{BSA}}} \quad (\text{S6})$$

By assuming that $P(t)$ increased to P_{BUCK} when $t = t_{\text{B}}$, and by using the boundary condition of $P(t_{\text{B}}) = P_{\text{BUCK}}$, we can derive t_{B} in the form of Equation S7:

$$t_{\text{B}} = R_{\text{EFF}} \times C_{\text{BSA}} \times \ln \left[\frac{(P_{\text{EFF}} - P_{\text{UNFOLD}})}{(P_{\text{BUCK}} - P_{\text{EFF}})} \right] \quad (\text{S7})$$

During unfolding, air flows from the bladder of the buckling-sheet inverter (C_{BSA}) to the atmosphere (P_{ATM}) through the pneumatic resistors (R_{TUBE} and R_{PULL}) (**Fig. S7B**). Equation S8 from the analogous electronic RC circuit describes the time varying pressure $P(t)$ inside the bladder of the buckling-sheet inverter during unfolding:

$$\frac{dP}{dt} = \frac{1}{(R_{\text{TUBE}} + R_{\text{PULL}}) \times C_{\text{BSA}}} \times (P_{\text{ATM}} - P(t)) \quad (\text{S8})$$

By solving the Eq. (S8) with the boundary condition of $P(t \rightarrow \infty) = P_{\text{ATM}}$, we derived the solution shown in Equation S9 for $P(t)$:

$$P(t) = (P_{\text{EFF}} - P_{\text{ATM}}) \times \exp\left[-t/(R_{\text{EFF}}^* \times C_{\text{BSA}})\right] + P_{\text{ATM}} \quad (\text{S9})$$

Where $R_{\text{EFF}}^* = R_{\text{TUBE}} + R_{\text{PULL}}$ is the simplified form of R_{EFF} for the unfolding RC circuit, when R_{BSA} is infinite due to the kinking of the flow-control tube.

By assuming that $P(t)$ decreased to P_{UNFOLD} when $t = t_{\text{U}}$ and using setting the boundary condition for the oscillation, $P(t_{\text{U}}) = P_{\text{UNFOLD}}$, we can derive t_{U} as Equation S10:

$$t_{\text{U}} = R_{\text{EFF}}^* \times C_{\text{BSA}} \times \ln\left[\frac{(P_{\text{EFF}} - P_{\text{ATM}})}{(P_{\text{UNFOLD}} - P_{\text{ATM}})}\right] \quad (\text{S10})$$

The oscillation period of a BRO containing n buckling-sheet inverters is therefore the sum of the buckling times (t_{B}) and unfolding times (t_{U}) of all n inverters (Eq. (S11), which is Eq. (3) in the main text):

$$t_{\text{PERIOD}} = n \times (t_{\text{B}} + t_{\text{U}}) \quad (\text{S11})$$

Furthermore, we modeled the amplitude of oscillation (A) by subtracting the minimum output pressure value from the maximum pressure during the oscillation. The maximum pressure calculated by taking time infinite in Eq. (S4) is given as $P(t \rightarrow \infty)$:

$$P(t \rightarrow \infty) = \frac{P_{\text{SUPP}} \times R_{\text{PULL}} + P_{\text{ATM}} \times R_{\text{BSA}}}{R_{\text{PULL}} + R_{\text{BSA}}} = P_{\text{EFF}}$$

We approximated the minimum pressure value as P_{UNFOLD} from experimental observation and derived the analytical expression for the amplitude of the oscillation as Equation S12:

$$A = P_{\text{EFF}} - P_{\text{UNFOLD}} \quad (\text{S12})$$

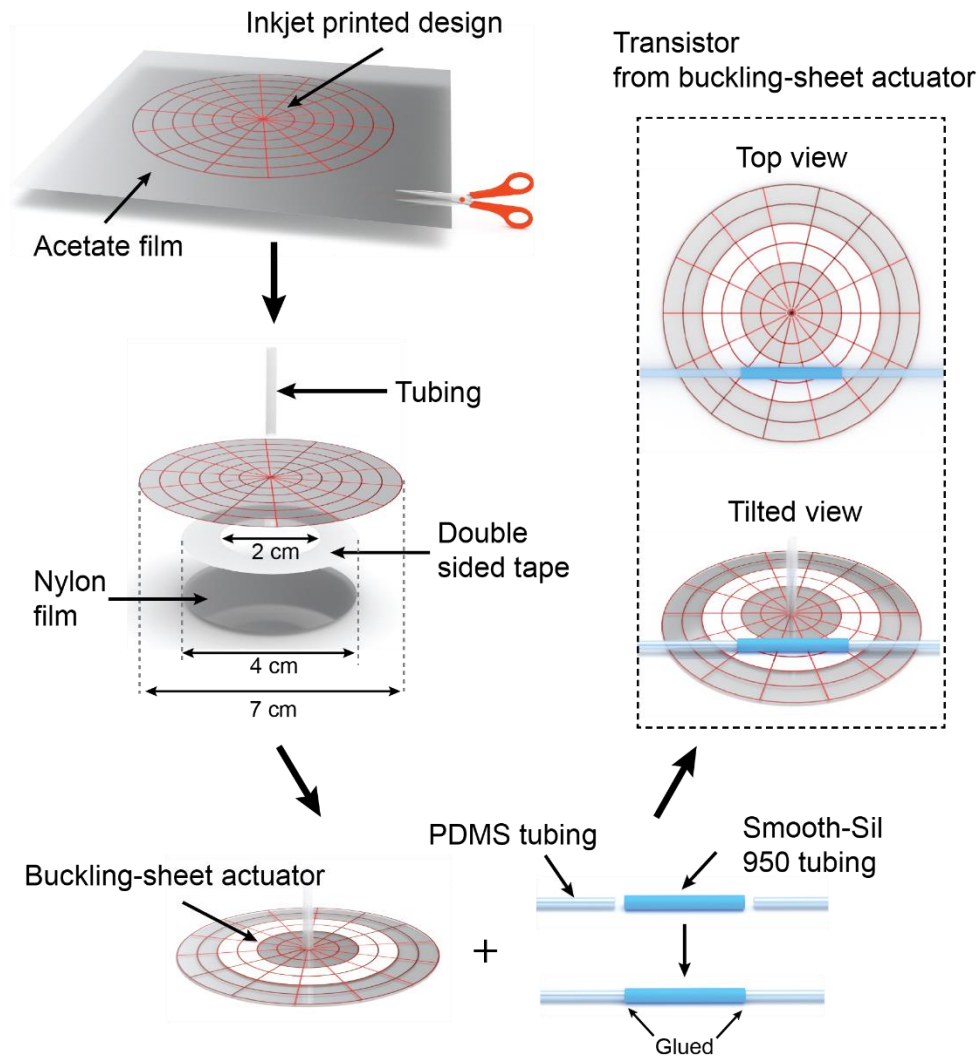


Fig. S1. Fabrication of the pneumatic switch based on buckling-sheet actuator. The circular design with the red stripes of the buckling-sheet actuator was inkjet printed on a poly(cellulose acetate) sheet, and the sheet was cut with a laser cutter or scissors. Then, a circular pneumatic bladder of Nylon film was attached at the center of the designed acetate sheet with double-sided tape. Thin rubber tubing connects the bladder to an external pneumatic source. To fabricate a pneumatic switch and inverter from the buckling sheet, a pneumatic flow-control tube was attached on the surface of buckling sheet, across the buckling position.

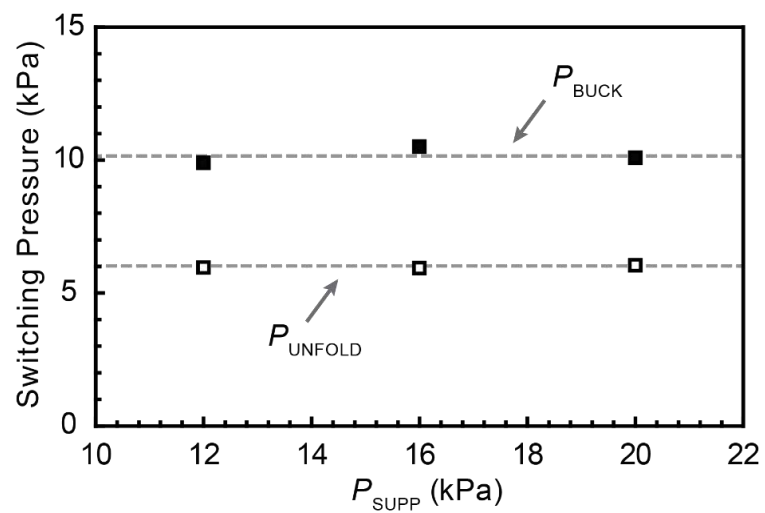


Fig. S2. P_{SUPP} does not influence the critical pressures. The critical switching pressures, P_{BUCK} and P_{UNFOLD} , were shown experimentally to be independent of the supply pressure, P_{SUPP} .

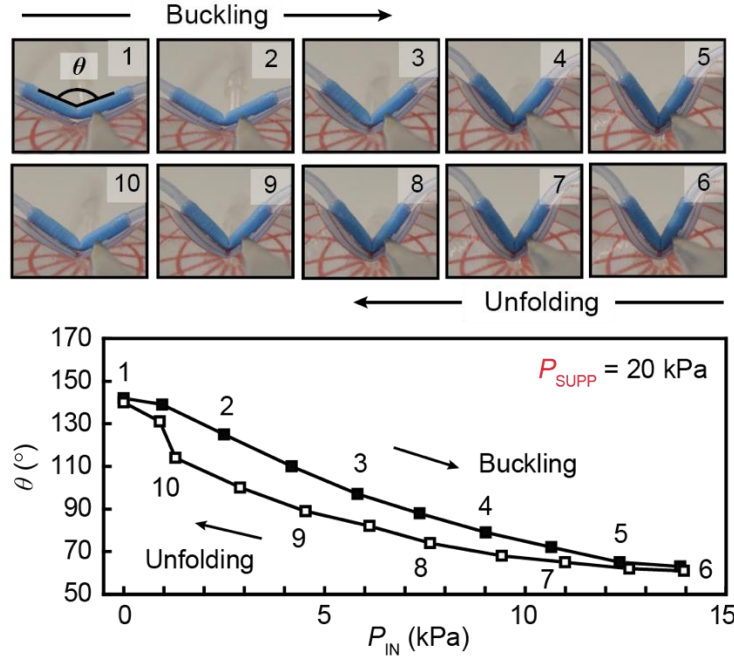


Fig. S3. Switching behavior of buckling-sheet inverter with geometric hysteresis. The bending angle (θ) of the pneumatic flow-control tube at the center of the buckling position was measured during invert switching of buckling-sheet inverter with P_{SUPP} of 20 kPa. During the buckling process, θ decreased with input pressure, P_{IN} , from $\theta = 145^\circ$ to $\theta = 75^\circ$ when the tube completely kinks and prevents the flow of air (stage 1 to 4). Then, θ further decreased as P_{IN} increased beyond P_{BUCK} down to a minimum value of $\theta = 60^\circ$ (stage 6). As the buckling-sheet inverter unfolds, θ increases from the minimum value to 90° as P_{IN} decreases to P_{UNFOLD} (stage 9). The θ values during unfolding are always smaller than those during buckling with the same P_{IN} (stage 10), giving rise to the geometric hysteresis.

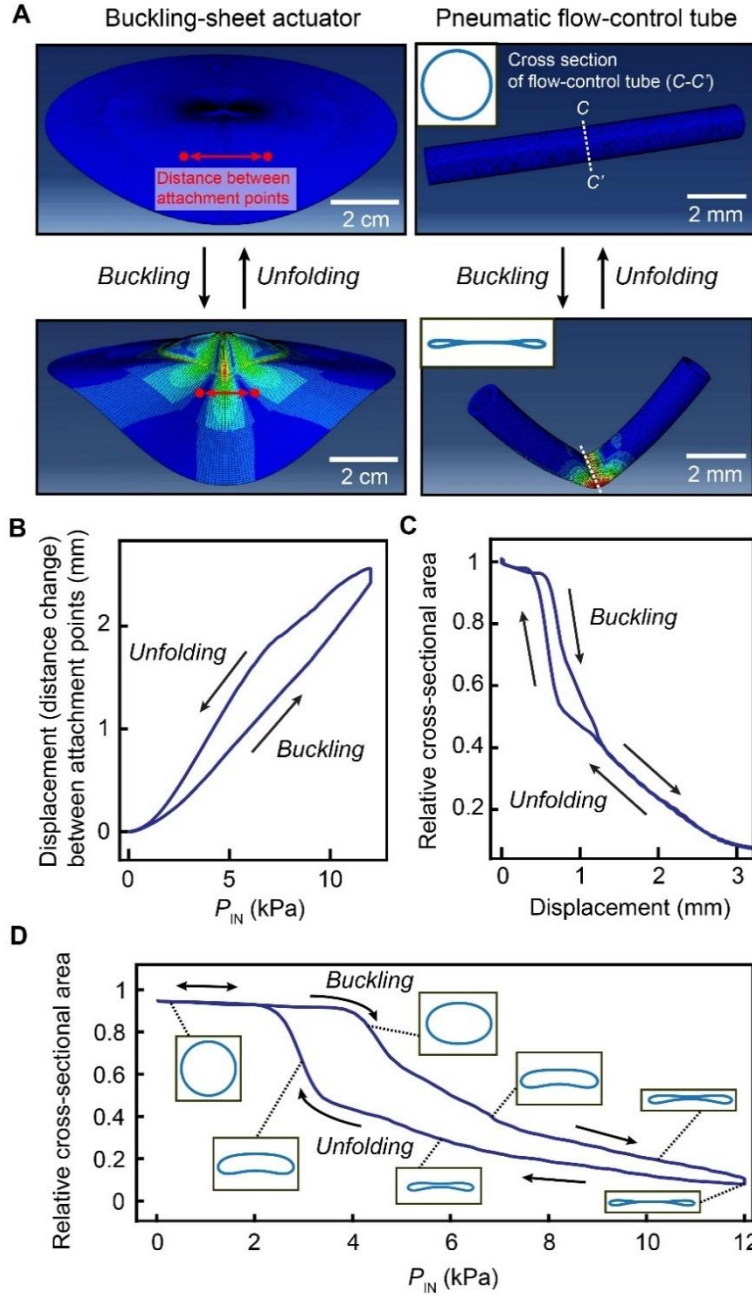


Fig. S4. Finite element method (FEM) models of the buckling-sheet inverter. Captured FEM images of the buckling-sheet actuator (left) and the attached pneumatic flow-control tube (right) (A). From the FEM of the buckling-sheet actuator, the displacement (or distance change) between attachments points of the tubing, i.e. between the red points in (A), was calculated as a function of input pressure (P_{IN}) to the bladder during the buckling and unfolding of the sheet (B). From the FEM model of the flow-control tube, the relative cross-sectional area at the center of the tube was estimated by inserting the displacement values from (B) into the model (C). The global behavior of the buckling-sheet inverter showed that the cross-sectional deformation of the central part of the tube varied with P_{IN} with hysteresis behavior similar to that observed during experiments (D).

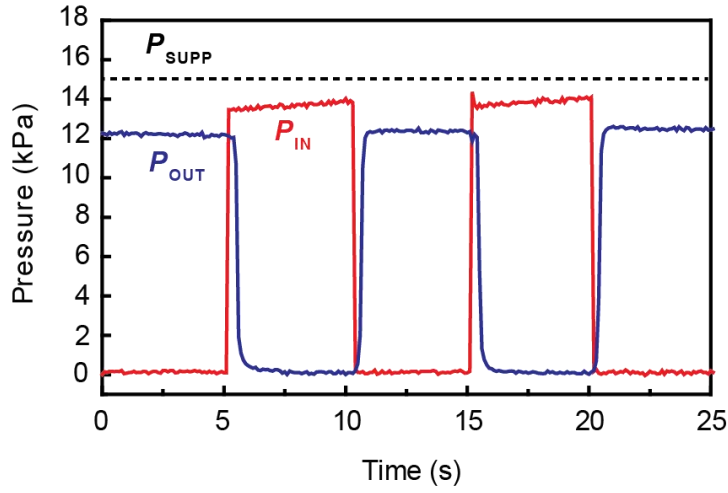


Fig. S5. Characterization of the buckling-sheet inverter by alternating P_{IN} . When the signal of P_{IN} is applied to the buckling-sheet inverter with a time interval of 5 s on and 5 s off under constant P_{SUPP} , the buckling-sheet inverter inverts the input signal, with P_{OUT} taking the opposite value of the input (a high output from a low input, and vice-versa). The P_{OUT} was lower than P_{SUPP} because of the pressure drop associated with the pulldown resistor.

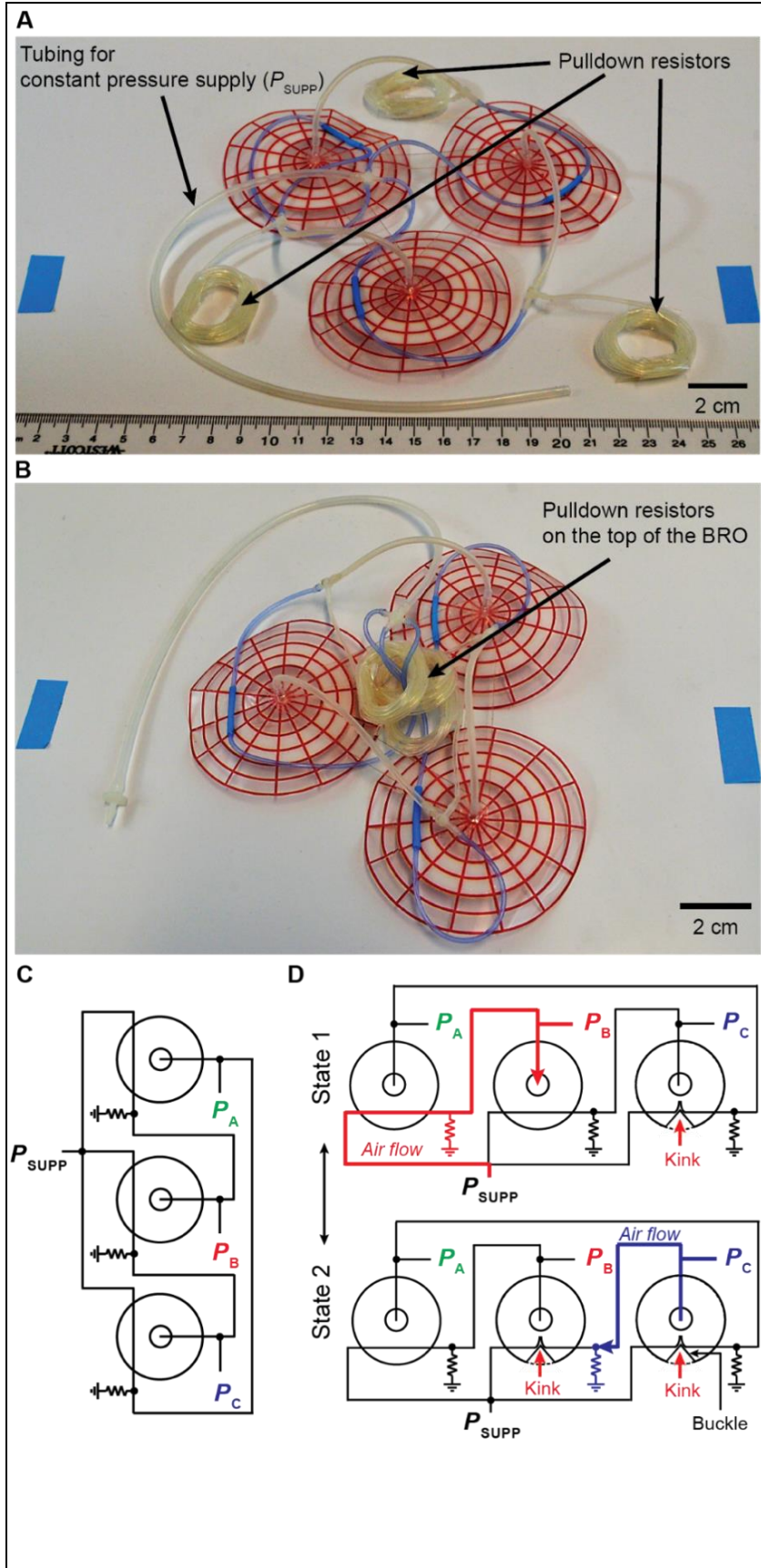


Fig. S6. Assembly of BRO and operating mechanism.

The photo of a BRO-based system shows three buckling-sheet inverters connected in a loop, where P_{OUT} of one constituent inverter acts as P_{IN} of the next inverter. To create the “ring,” P_{OUT} from the last inverter in the series is connected to P_{IN} of the first inverter (**A**). For locomotion, the pulldown resistors were loaded on the top of the BRO (**B**). A corresponding pneumatic circuit analog shows formation of a ring oscillator using three pneumatic inverters (disks) and pulldown resistors grounded with atmospheric pressure (**C**). When P_{SUPP} is first applied to the system, no stable state exists for the oscillation, but after a period of ~ 2 s, a pneumatic instability forms and travels around the ring as inverters sequentially buckle and unfold. The ring oscillator always contains either two adjacent unfolded inverters (with one inverter buckling, shown in state 1), or two adjacent buckled inverters (with one inverter unfolding, shown in state 2) (**D**).

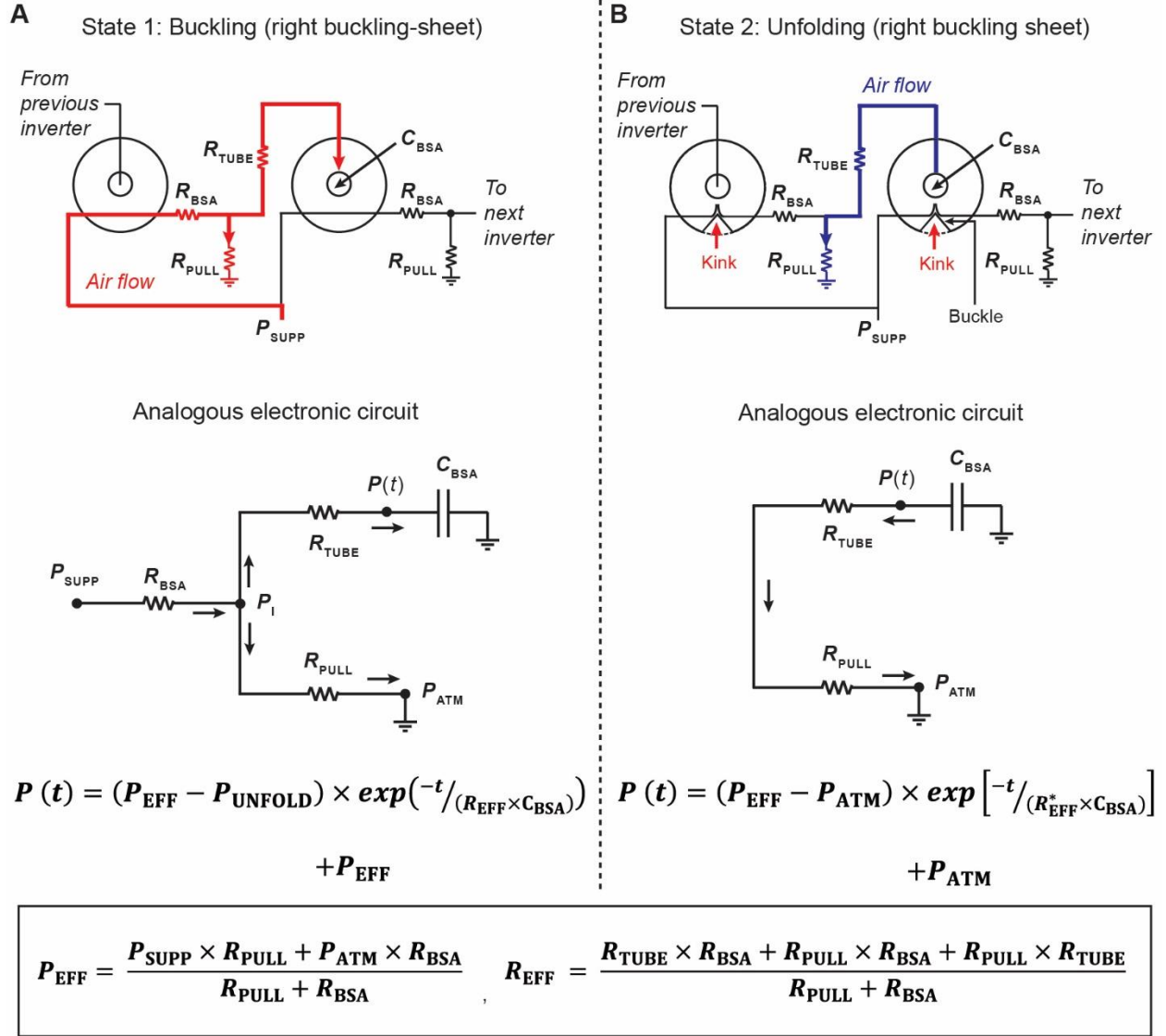


Fig. S7. Analytical model for a BRO based on an electronic RC circuit analog. Pneumatic and analogous electronic RC circuits, with the analytical solutions of time varying pressure inside the buckling-sheet inverter, $P(t)$, for both states during buckling (**A**) and unfolding (**B**). The circuit shown in (**B**) does not have a connection to the left side, towards the supply pressure, because it is adjacent to a buckling-sheet inverter in the buckled state preventing a pneumatic connection. The solutions were derived using boundary conditions for the oscillation as described in the Supplementary Text.

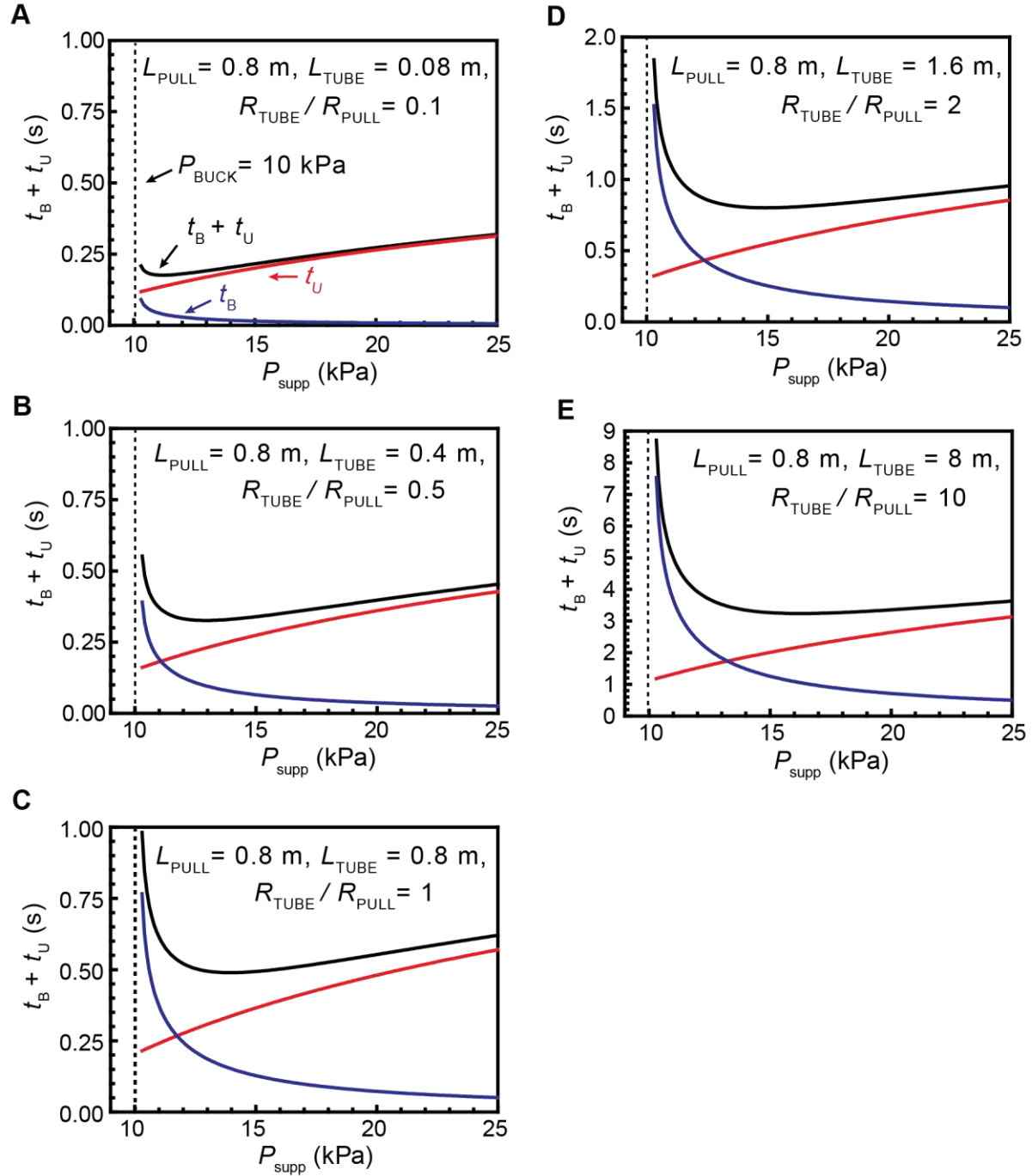


Fig. S8. Oscillation period vs. P_{SUPP} with varying pneumatic parameters. The period predicted from the model, shown here as the sum of buckling time (t_B) and unfolding time (t_U), as a function of P_{SUPP} with different pneumatic resistor ratios of $R_{\text{TUBE}}/R_{\text{PULL}}$ of 0.1 (A), $R_{\text{TUBE}}/R_{\text{PULL}} = 0.5$ (B), $R_{\text{TUBE}}/R_{\text{PULL}} = 1$ (C), $R_{\text{TUBE}}/R_{\text{PULL}} = 2$ (D), and $R_{\text{TUBE}}/R_{\text{PULL}} = 10$ (E).

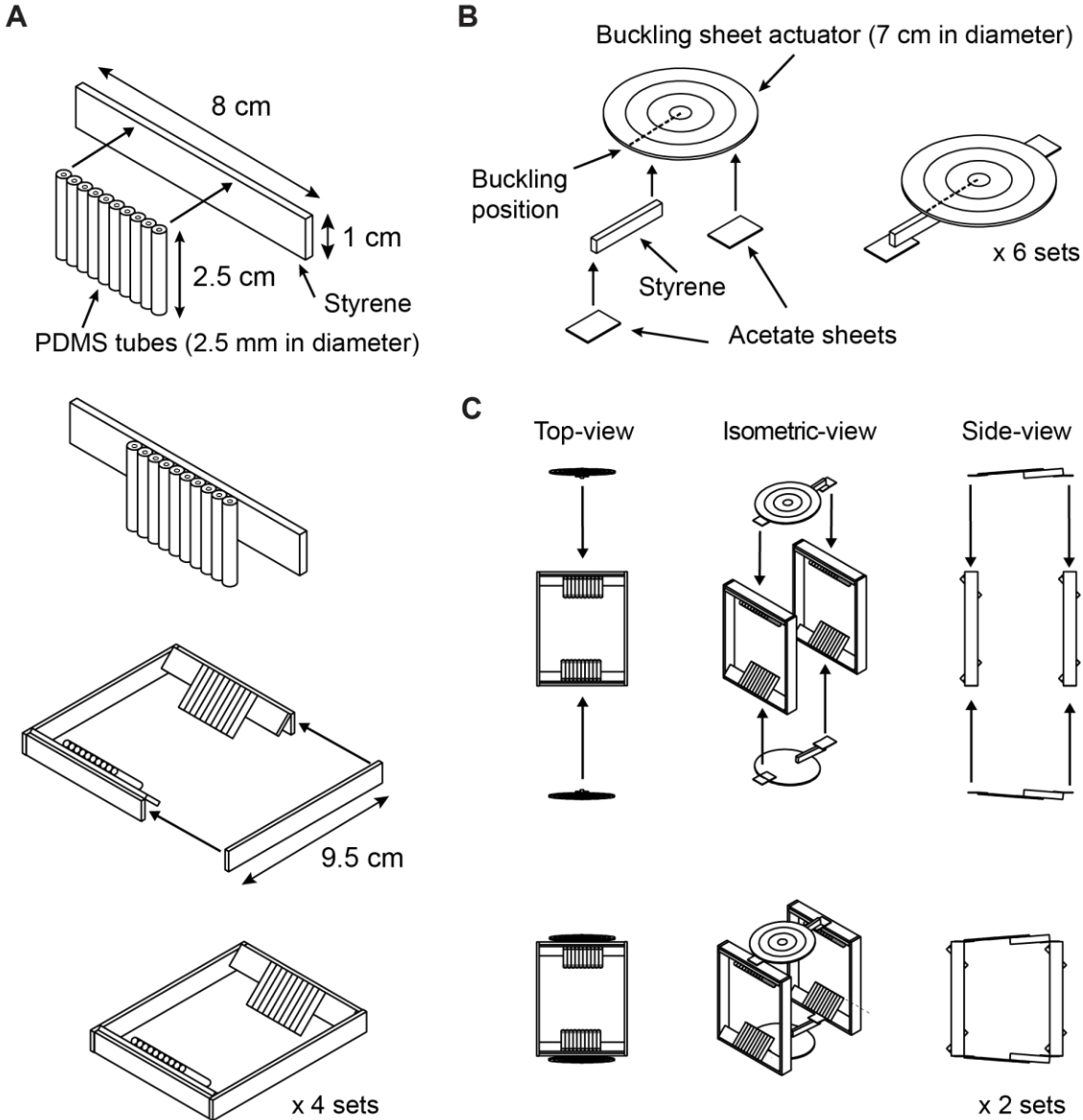


Fig. S9. Design and assembly of the beam-climber robot (steps 1-3). PDMS tubes were attached to a length of styrene with super glue to form each “foot” that contacts the beam. Then this length was glued into a rectangular frame (with hot glue) such that the PDMS tubes could contact a beam at a 45° angle, resulting in asymmetric friction behavior of each foot (**A**). Six actuators were constructed by gluing a thin piece of styrene along the “programmed” buckling point (folded by hand) in the buckling sheet actuator. Acetate sheets were then attached to the length of styrene and the other side of the buckling sheet actuator to be used as mounting points (**B**). A pair of actuators were connected to two frames, taping the acetate mounting points to the frames. This process was repeated with the remaining two frames and a second pair of actuators (**C**).

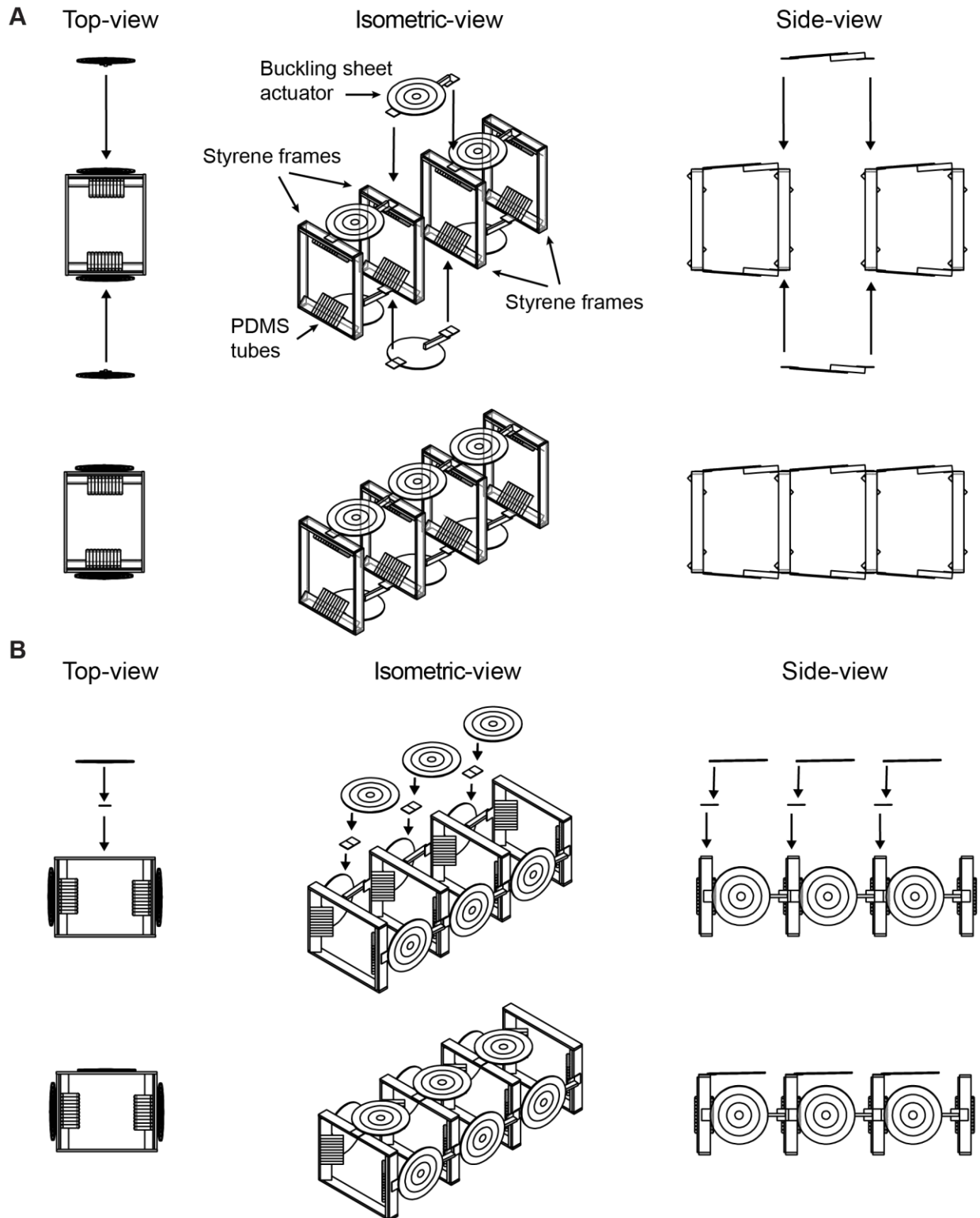


Fig. S10. Design and assembly of the beam-climber robot (steps 4-5). The two sections shown in Fig. S9C were connected using the two remaining actuators by taping the acetate mounting points to the two frames (A). The BRO was then attached to the robot by taping its constituent buckling-sheet inverters to the front three frames using double-sided tape (B).

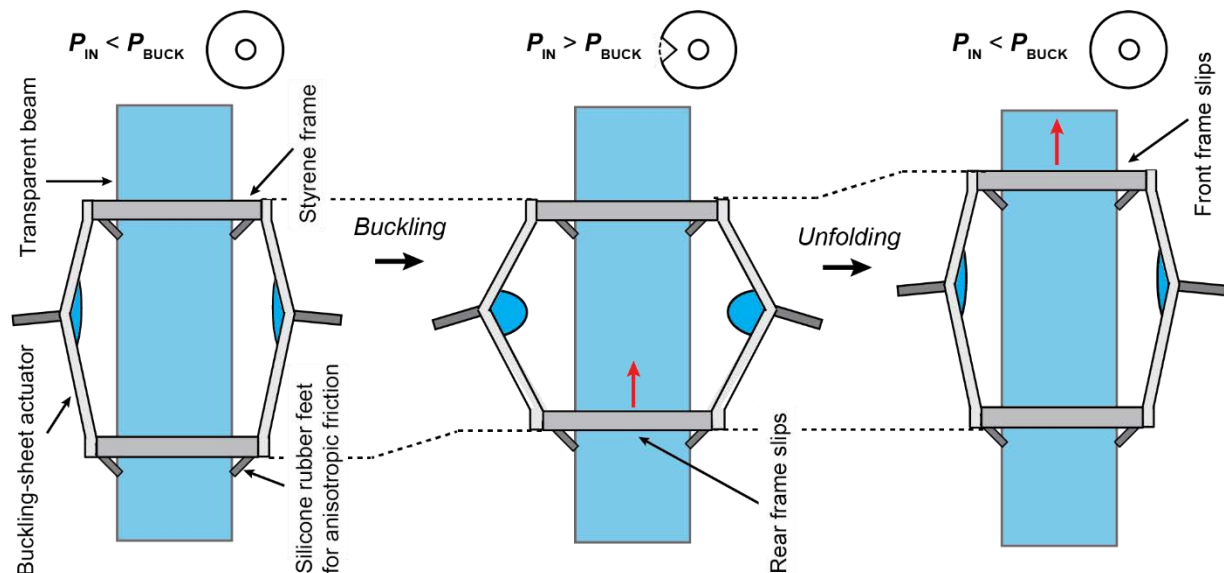


Fig. S11. Schematic illustration of beam climbing process. Each of the three unit cells of the beam-climber robot achieves climbing behavior as shown: (i) when the internal buckling-sheet actuator (BSA) pressure increases above P_{BUCK} , the BSA contracts in the vertical direction, but only the lower frame is able to move due to the asymmetric friction at the feet contacting the beam (center image); (ii) then, when the internal buckling-sheet actuator (BSA) pressure decreases below P_{BUCK} , the BSA extends in the vertical direction, but only the upper frame is able to move, again due to the asymmetric friction at the feet contacting the beam (right image). These oscillations in pressure within each of the three units of the beam-climber robot are driven by each the three outputs of the BRO, respectively.

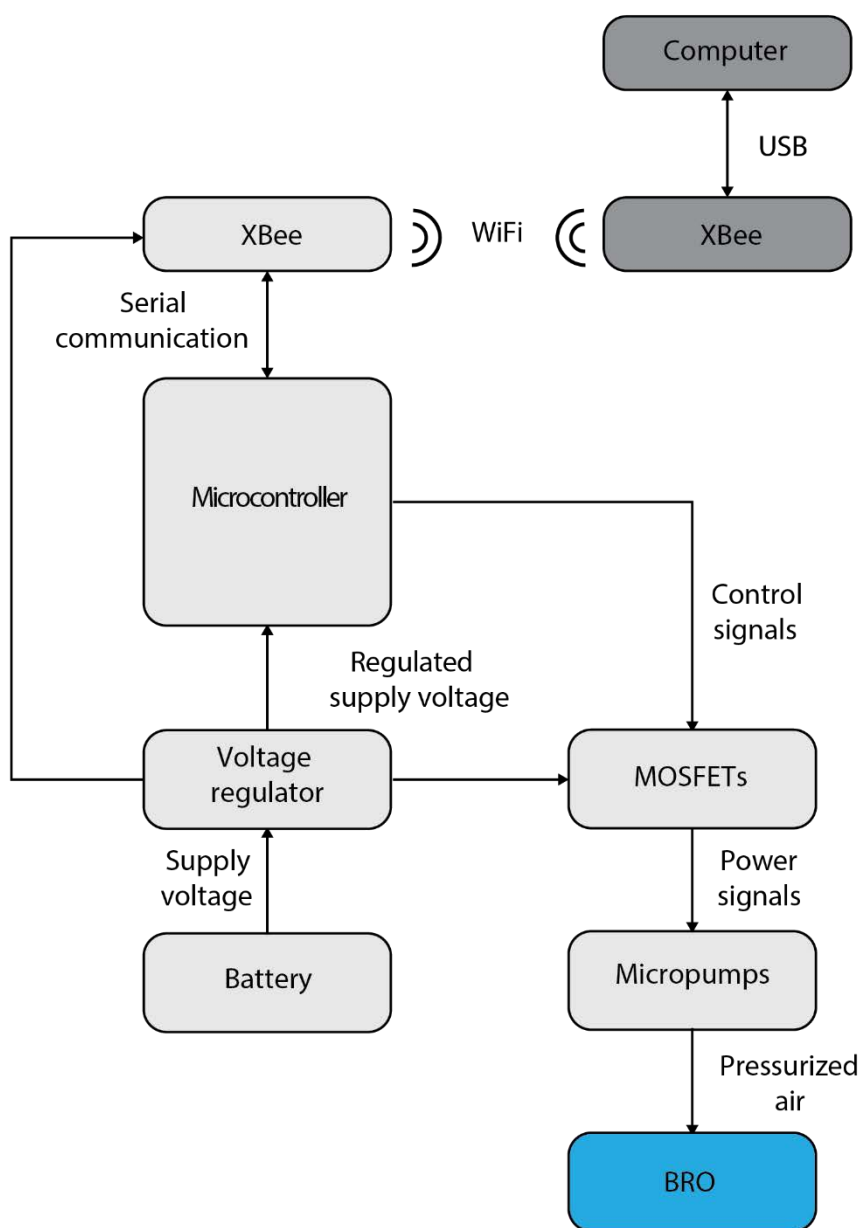


Fig. S12. Circuit design for untethered BRO. This schematic shows the individual components of our custom-made circuit used to operate BRO. A lithium-ion battery is connected to a voltage regulator, and the regulator supplies a constant voltage to the electronics. A microcontroller enables communication with a computer via X-Bee modules to switch two micropumps using a dual-channel MOSFET circuit.

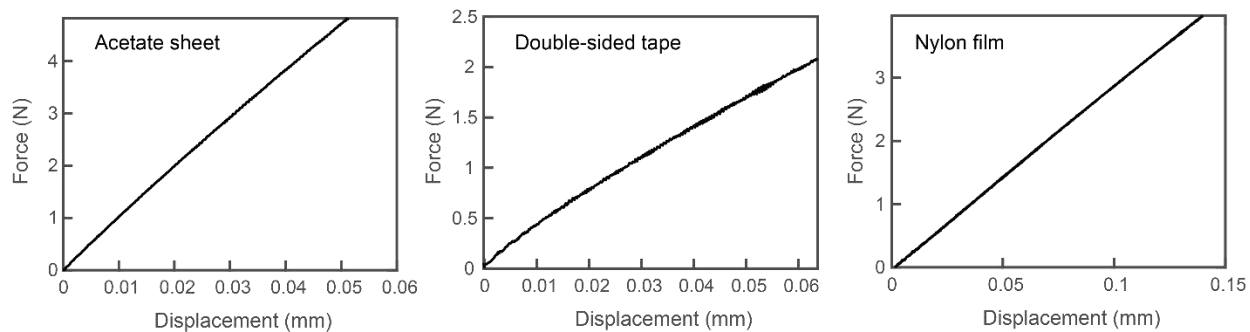


Fig. S13. Tensile tests on the materials. A linear regression was performed on the tensile data to determine Young's moduli of the different materials with values: 2.13GPa (acetate sheet), 0.32GPa (double-sided tape), 2.35GPa (Nylon film).

Table S1: Initial dimension of the tensile test specimens.

Material	Width (mm)	Length (mm)	Thickness (mm)
Acetate sheet	12.4	25.3	0.09
Double-sided tape	12.4	25.3	0.2
Nylon film	12.4	25.3	0.025

Table S2: Summary of all abbreviations in the main text.

Abbreviations	Meaning in the main text
BSA	Buckling-sheet actuator
BRO	Buckling-sheet ring oscillator
P_{IN}	Input pressure to the bladder of a buckling-sheet actuator
P_{BUCK}	Upper threshold value of input pressure (P_{IN}) for the complete buckling of a buckling-sheet actuator
P_{UNFOLD}	Lower threshold value of input pressure (P_{IN}) for the unfolding of a buckling-sheet actuator
P_{SUPP}	Constant supply pressure at the inlet of the flow-control tube
P_{OUT}	Variable output pressure at the outlet of the flow-control tube
P_{ATM}	Atmospheric pressure (pneumatic ground)
P_{EFF}	The effective pressure of the pneumatic circuit for a buckling-sheet ring oscillator
R_{EFF}	The effective resistance of the pneumatic circuit for a buckling-sheet ring oscillator
R_{PULL}	The pneumatic resistance from the pulldown resistor
R_{TUBE}	The inter-device pneumatic resistance
R_{BSA}	The pneumatic resistance from the flow control tube on a buckling-sheet actuator
C_{BSA}	The pneumatic capacitance of a buckling-sheet actuator
t_B	The buckling time for a buckling-sheet inverter
t_U	The unfolding time for a buckling-sheet inverter

Movie S1.

FEM for buckling-sheet actuator.

Movie S2.

FEM for the pneumatic flow-control tube attached on the buckling-sheet actuator.

Movie S3.

Translational motion of BRO.

Movie S4.

Rotational motion of BRO.

Movie S5.

Hybrid motions of twinned BROs.

Movie S6.

Crawling motion of BRO on sand.

Movie S7.

Swimming motion of BRO on water surface.

Movie S8.

Untethered motion of BRO on pool table.

Movie S9.

Motion of beam climber robot (0° tilting of the beam).

Movie S10.

Motion of beam climber robot (45° tilting of the beam).

Movie S11.

Motion of beam climber robot (90° tilting of the beam).

Movie S12.

Diving motion of beam climber robot with underwater cleaning.